“© 2022 IEEE. Personal use of this material is permitted. Permission from IEEE must be obtained for all other uses, in any current or future media, including reprinting/republishing this material for advertising or promotional purposes, creating new collective works, for resale or redistribution to servers or lists, or reuse of any copyrighted component of this work in other works.”

This article has been accepted for publication in IEEE Sensors Journal. This is the author's version which has not been fully edited and content may change prior to final publication. Citation information: DOI 10.1109/JSEN.2022.3192088

Effect of Phononic Crystal Orientation on AlN-on-Silicon Lamb Wave Micromechanical Resonators

Renhua Yang, Yiwen Zhang, Jingui Qian, and Joshua E.-Y. Lee, *Senior Members, IEEE*

***Abstract*—Phononic crystals (PnCs) have been used to boost the quality factor (Q) of AlN-on-Silicon Lamb Wave Resonators (LWRs). But most reports on applying PnCs to resonators have focused on the common <110> orientation within (100) silicon. Little is known on the applicability of other crystal orientations. In this work, we explore the effect of orientation on the acoustic band gap (ABG) of two PnC designs and their effect on boosting Q: a disk PnC and a ring PnC. From Finite Element simulation, we show that the disk PnC's ABG is insensitive to orientation while adding a hole into the disk to form a ring changes its ABG to be much more sensitive to orientation. Leveraging the PnCs as anchoring boundary of LWRs, the disk PnC exhibits comparable effectiveness to boost Q > 11,000 in the <110> and <100> directions while the ring PnC is effective only in the <110> direction. We further corroborate these trends by incorporating the disk PnC into delay lines in either crystal axis.**

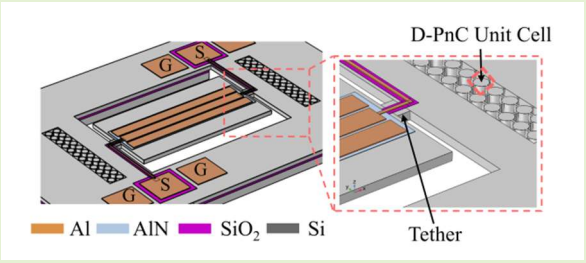

***Index Terms*— Phononic crystal; Orientation; Piezoelectric resonator; Lamb wave; Delay line**

I. Introduction

Microelectromechanical Systems (MEMS) resonators have emerged as a promising alternative to quartz crystals in timing applications [1-7]. For oscillator applications, high quality factor (Q) and low motional resistance (R_m) are desired for low phase noise [8-12]. Capacitive resonators can deliver Qs on par with quartz crystals but are limited in their application at higher frequency ranges as high bias voltages are required to reduce an intrinsically large motional resistance (R_m) [13-17]. By contrast, thin-film piezoelectric-on-substrate (TPoS) resonators comprise an AlN film for piezoelectric transduction and a thicker low acoustic loss substrate like silicon [18-23]. TPoS resonators combine the advantages of piezoelectric transduction to deliver low R_m while also having higher Q and power handling from the thick substrate. Besides, TPoS fabrication allows the flexibility to engineer the properties of the substrate to improve the performance of the resonator. For instance, nonlinearity in TPoS resonators can be reduced by tuning the doping concentration and aligning the resonator to the <100> orientation of the silicon substrate [24]. In addition, it has been shown that the temperature coefficient of frequency (TCF) of a TPoS resonator can be significantly lowered by fabricating on degenerately doped silicon and aligned to the <100> orientation [25].

TPoS resonators can have moderately high Qs with careful design to minimize damping, of which anchor loss is rather common to TPoS resonators [26-27]. Among the various approaches to reduce anchor loss in AlN-on-Si piezoelectric resonators [28-34], phononic crystals (PnCs) are an interesting approach for confining acoustic waves within the resonator to boost Q. Most results on the use of PnCs for boosting Q in resonators have been based on the commonly used <110> axis of (100) Si. Little is known on the application of PnCs in alternative crystal orientations (e.g. <100>) that could be beneficial for other aspects of performance such as lower TCF or higher linearity. Given that Si is anisotropic, changing the orientation of the PnC will generally affect the characteristics of the acoustic band gap (ABG) [35-40] and thus effectiveness in boosting Q.

In this work, we explored the effect of orientation on the acoustic band gap (ABG) of two PnC designs, which will further affect their Q-boosting effectiveness for very high frequency (VHF) band Lamb wave resonator (LWRs) aligned

Submitted: 10 May 2022. The work described in this paper was supported Research Grant Council (RGC) General Research Fund (GRF) with the RGC project number 11218118. Corresponding author: Jingui Qian; Renhua Yang.

Renhua Yang is with department of Mechanical Engineering, City University of Hong Kong, Kowloon, Hong Kong SAR, China (e-mail: rhyang2-c@my.cityu.edu.hk).

Yiwen Zhang is with department of Electrical Engineering, City University of Hong Kong, Kowloon, Hong Kong SAR, China (e-mail: yzhang2544-c@my.cityu.edu.hk).

Jingui Qian is with Anhui Province Key Laboratory of Measuring Theory and Precision Instrument, School of Instrument Science and Opto-Electronics Engineering, Hefei University of Technology, Hefei, Anhui, China. (e-mail: jgqian@hfut.edu.cn).

Joshua E.-Y. Lee was with Department of Electrical Engineering, City University of Hong Kong, Hong Kong SAR, China (email: joshlee@cantab.net).

XXXX-XXXX © XXXX IEEE. Personal use is permitted, but republication/redistribution requires IEEE permission.
See http://www.ieee.org/publications_standards/publications/rights/index.html for more information.
© 2022 IEEE. Personal use is permitted, but republication/redistribution requires IEEE permission. See https://www.ieee.org/publications/rights/index.html for more information.

This article has been accepted for publication in IEEE Sensors Journal. This is the author's version which has not been fully edited and content may change prior to final publication. Citation information: DOI 10.1109/JSEN.2022.3192088

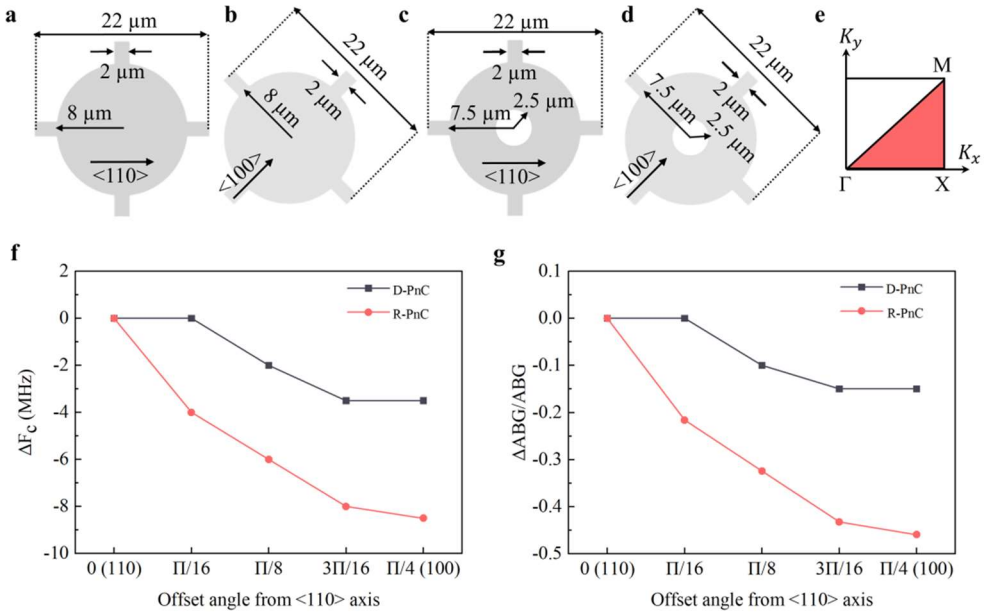

FIG. 1. Top view schematic of a D-PnC unit cell aligned along the (a) <110> and (b) <100> directions. Top view schematic of a R-PnC unit cell aligned along the (c) <110> and (d) <100> directions. (e) 1st irreducible Brillouin zone in k-space. (f) Change in the center frequency (f_c) of the acoustic bandgap (ABG) as a function of the alignment between the <110> and <100> direction within the (100) plane and (g) corresponding fractional change in the size of the bandgap ($\Delta f_{BG}/f_{BG}$) illustrating a larger effect from the R-PnC (45% reduction) over the D-PnC (15% reduction).

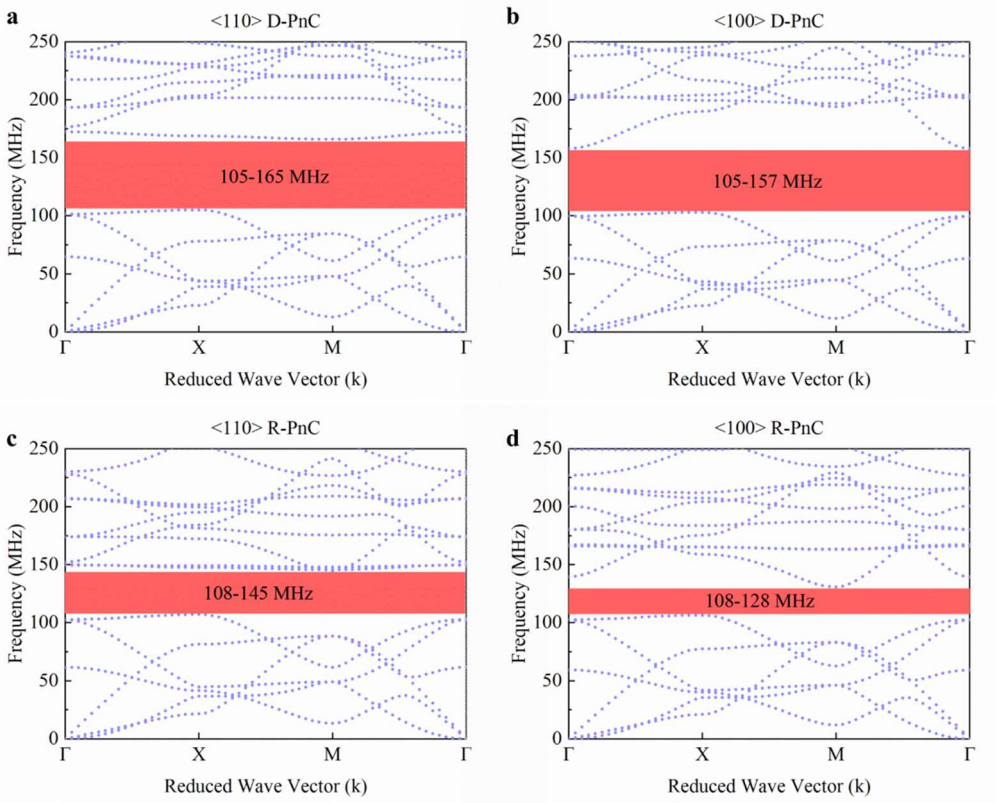

FIG. 2. Simulated frequency band diagrams for the D-PnC aligned along the (a) <110> and (b) <100> directions. Simulated frequency band diagrams for the R-PnC aligned along the (c) <110> and (d) <100> directions.

to the <110> and <100> directions within the (100) plane. The PnC topologies are based on a disk PnC (D-PnC) and a ring PnC (R-PnC). Finite element (FE) simulations show that the D-PnC and R-PnC show different sensitivities to the change in orientation. As a unique case, the ABG size of the D-PnC does not change significantly from one orientation to the other. By contrast, simply adding a hole in the D-PnC to form an R-PnC causes the ABG to significantly shrink when rotating from the <110> to the <100> direction. In addition to the simulation, we fabricate the PnCs into LWRs and delay lines to examine the orientation effect on ABG to boost Q. We show that D-PnCs are equally effective in both the <110> and <100> directions

© 2022 IEEE. Personal use is permitted, but republication/redistribution requires IEEE permission. See https://www.ieee.org/publications/rights/index.html for more information.

This article has been accepted for publication in IEEE Sensors Journal. This is the author's version which has not been fully edited and content may change prior to final publication. Citation information: DOI 10.1109/JSEN.2022.3192088

which attain similar levels of recorded high Q [31] while R-PnCs were far less effective in <100> orientation. Moreover, D-PnCs can also provide equally significant attenuation within the ABG when incorporated into delay lines, which further corroborates its excellent effectiveness in Q-boosting for LWRs aligned to either orientation.

II. SIMULATION: EFFECT OF ORIENTATION ON THE ACOUSTIC BANDGAP

The D-PnC and R-PnC unit cell with detailed dimensions described in this work are shown in Fig. 1(a-d). The thickness of both PnCs is defined by a 10 µm silicon layer. We computed the ABG diagram of the PnCs along different crystal orientations within the (100) plane in Si using COMSOL 5.3. For the boundary conditions, we applied Floquet periodic conditions along the x and y directions in each PnC unit domain. Fig. 1(e) illustrates the swept wave vector k bounding the first Brillouin zone. To characterize the effect of orientation on the ABG, we simulated for various orientations between the <110> axis to the <100> axis (45° to the <110> axis) by sweeping the corresponding Euler angles (α,0,0) from (π/4,0,0) to (0,0,0) in steps of (π/16,0,0). The center frequencies (f_c) of the ABGs associated with the D-PnCs and R-PnCs along the <110> orientation were both designed to be around 130 MHz. Fig. 1f illustrates the effect of orientation on the center frequency, where Δf_c denotes the resulting shift in f_c. Fig. 1(g) shows the corresponding effect of orientation on the size of the bandgap (f_{BG}) where Δf_{BG} denotes the resulting change in the size of the bandgap. Rotating from <110> to <100>, D-PnCs see a slight reduction within 15% in f_{BG}, and 3% downshift in f_c. In contrast, the R-PnC sees a far more significant reduction in the f_{BG} by over 45% and a larger downshift by f_c by 7%. We also computed for the GHz and kHz range by scaling the dimensions, and the results are consistent with VHF range. As such, from the simulations, the ABG associated with the D-PnC is rather unique in orientation-insensitivity. Simply adding a hole into D-PnC forming an R-PnC changes the characteristic quite substantially. As shown in [35], the ABG is highly dependent on the constituent materials, especially the contrast between density and elastic constants of the inclusions and the matrix, the geometry of inclusions, the inclusion shape and the fill factor. Despite having the same shape, the D-PnC and R-PnC have two key differences. On one hand, the D-PnC has the matrix of air/silicon and the R-PnC has the matrix of air/silicon/air. On the other hand, the D-PnC has a larger fill factor than the R-PnC. To some extent, the simpler matrix and larger fill factor may weaken the effect of orientation.

We further simulated the frequency band diagrams of D-PnCs and R-PnCs along the two main orientations: <110> and <100> as depicted in Fig. 2. For D-PnCs shown in Fig. 2(a) and Fig. 2(b), we can observe that it has a wide ABG from 105-165 MHz with f_c around 135 MHz along the <110> direction, and also an equally wide ABG from 105-157 MHz with f_c around 131 MHz along the <100> orientation, which has a slight difference in the f_{BG} width and f_c among these two orientations. In contrast, the change in ABG characteristics is much significant for the R-PnC as shown in Fig. 2(c) and Fig. 2(d). We can see that it has a wide ABG spanning from 108-145 MHz with f_c around 127 MHz along the <110> direction. But the ABG narrows down to 108-128 MHz with f_c shifting down to 118 MHz along the <100> direction, which has an obvious difference in the f_{BG} width and f_c among these two orientations. Thus, we can see the effect of orientation on the ABG of PnCs has a visible difference between different geometries. As expected, orientation in an anisotropic material like Si would notably affect the ABG characteristics as can be seen in the case of the R-PnC. The orientation-insensitivity seen in the D-PnC is likely an exception to the rule.

III. EXPERIMENTAL VERIFICATION: PNCS APPLIED TO LWRS ALIGNED ALONG DIFFERENT ORIENTATIONS

We further fabricated the PnCs into AlN-on-Silicon LWRs as the anchoring boundaries to verify the effect of the PnCs to boost Q along different orientations. The devices in this work were all fabricated by a standard AlN-on-SOI MEMS process [41]. First, we fabricated and tested different number of rows (2 rows, 3 rows and 5 rows) of D-PnC unit cells at the anchoring boundaries of the LWRs along <110> orientation to find an optimal number of rows of unit cells by comparing the resulting Qs. Fig. 3(a) compares the admittance Y_{11} of the three LWRs resonators and Fig. 3(b) are the corresponding Y_{11} spectra after removing feedthrough due to the static capacitance C_0. We can see that these three LWRs display a similar high level of Q. To this end, we limited the numbers of rows of PnC unit cells to two for a more compact form factor and higher thermal nonlinearity limits owning to lower surface scattering [42]. The unloaded values of Q of all the LWRs herein were derived from

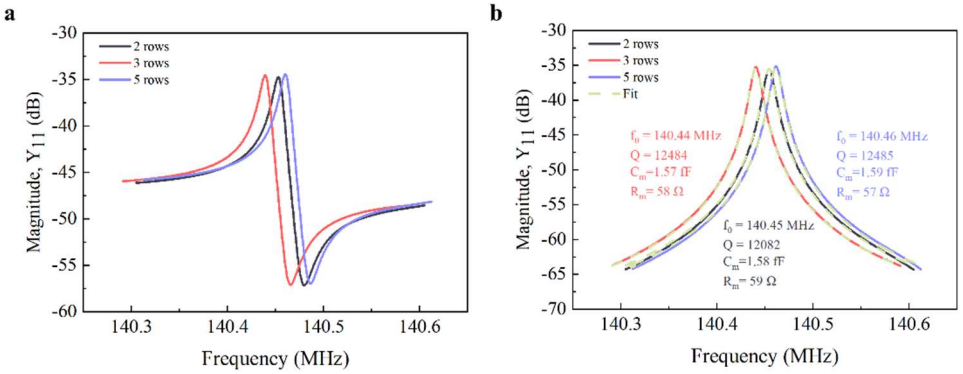

Fig.3. Admittance Y_{11} comparison of the LWRs with different rows of D-PnC as anchoring boundaries (a) before and (b) after removal of feedthrough due to static capacitance C_0.

© 2022 IEEE. Personal use is permitted, but republication/redistribution requires IEEE permission. See https://www.ieee.org/publications/rights/index.html for more information.

This article has been accepted for publication in IEEE Sensors Journal. This is the author's version which has not been fully edited and content may change prior to final publication. Citation information: DOI 10.1109/JSEN.2022.3192088

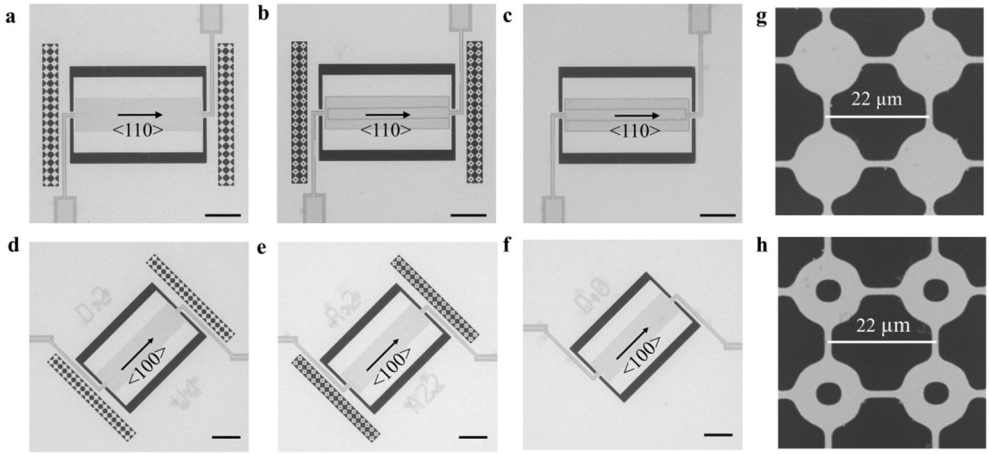

FIG. 4. SEM images of fabricated LWRs aligned to the <110> direction: a) LWR with D-PnC anchoring boundaries, b) LWRs with R-PnC anchoring boundaries, c) reference LWR with no PnCs at the anchor. (d-f) SEM images of fabricated the same set of three LWRs but aligned to the <100> direction. Scale bar: 100 µm. SEM images showing a zoom-in view of the g) D-PnC and h) R-PnC with a period or lattice constant of 22 µm.

one-port measurements of LWRs to obtain the S_{11}, from which the admittance Y_{11} was obtained. Q was then extracted by performing a model curve fit based on the modified Butterworth van Dyke model. All the one-port measurements of the LWRs were measured using an Agilent E5061A network analyzer connected through ground-signal-ground probes at ambient pressure and temperature. Open-short calibration was performed prior to all the one-port measurements to determine Q.

To simplify the comparison of the effectiveness in Q-boosting along different orientations, we initially set the D-PnC and the R-PnC to be equally effective by the design of the resonance frequency of LWRs for <110> orientation. We then characterized the orientation effect by comparing the effectiveness to boost Q of the same LWRs between the same set of PnCs for <100> orientation. To this end, the orientation is the only variant while the parameters of the PnCs and LWRs keep unchanged. Moreover, the LWRs were designed to be transduced in the 7th order width-extensional mode (140 MHz) for the <110> orientation, which lies well in the corresponding ABG of the D-PnC (105-165 MHz) and R-PnC (108-145 MHz) for the <110> orientation. The electrode pitch of the interdigitated transducer (IDT) in all the LWRs is 30 µm. Fig. 4(a)-(c) show three variants of the same LWR designed to align to the <110> direction. Fig. 4(a) shows an LWR bounded by D-PnCs, Fig. 4(b) shows the same LWR bounded by R-PnCs, and Fig. 4(c) shows the same LWR without PnCs as a reference device for comparison. Similarly, Fig. 4(d) to 4(f) show the same set of three variants but designed to align along the <100> direction. Fig. 4(g)-(h) depict zoom-in views of the PnCs. The respective resonant frequency ($f_{0,LWR}$) of 7th order width-extensional mode can be calculated from equations (1) and (2):

$$f_{0,LWR} = c/2W_p \quad (1)$$

$$c = \sqrt{E/\rho(1-\nu^2)} \quad (2)$$

where W_p is the pitch size of the electrodes, ρ is the density, E and ν are the Young's modulus and Poisson's ratio respectively. For Silicon, the Young's modulus is 169 GPa for the <110> orientation and 130 GPa for the <100> orientation. The Poisson's ratio is 0.064 for the <110> orientation and 0.28 for the <100> orientation. The density is 2329 kg/m^3.

The resonant frequency of LWRs is calculated to be 140 MHz for <110> orientation and 129 MHz for <100> orientation respectively, which are consistent with the FE simulations. The LWRs were designed to be only partially covered by IDTs, as seen from Fig. 4(a)-(c) to reduce the effect of electrode-related losses on Q. Fig. 5(a) and Fig. 5(b) compare the admittance Y_{11} of the three LWRs resonators (with D-PnC anchoring boundaries, R-PnC anchoring boundaries, and the reference with no PnC anchoring boundaries) along <110> and <100> orientation respectively. Fig. 5(c) and Fig. 5(d) are the corresponding Y_{11} spectra after removing feedthrough due to the static capacitance C_0. For the LWRs along <110> orientation illustrated in Fig. 5(c), the LWR with D-PnC anchoring boundaries demonstrates an unloaded Q of over 12000 which is 2.6 times of the reference LWR. The corresponding R_m is reduced by 87 Ω respectively, yielding a 4 dB decrease in insertion loss ($IL=20*\log_{10}[(R_m/2R_0)+1]$, R_0=50 Ω). The LWR with R-PnC anchoring boundaries shows a Q of 11700, which is 2.5 times of the reference LWR. As such, the degree of enhancement from incorporating the D-PnC and R-PnC is similar for <110> orientations. For LWRs along the <100> orientation shown in Fig. 5(d), the LWR with D-PnC anchoring boundaries has a Q of over 10000, which is about 2.4 times of the reference LWR. The corresponding R_m is reduced by 68 Ω, yielding a 3 dB decrease in insertion loss. The LWR with R-PnCs anchoring boundaries has a Q of 6890, which is 1.5 times of the reference LWR. Therefore, the R-PnC is less effective than the D-PnC in the Q-enhancement for LWRs along <100> orientations.

In addition, we also measured another two samples of each

© 2022 IEEE. Personal use is permitted, but republication/redistribution requires IEEE permission. See https://www.ieee.org/publications/rights/index.html for more information.

This article has been accepted for publication in IEEE Sensors Journal. This is the author's version which has not been fully edited and content may change prior to final publication. Citation information: DOI 10.1109/JSEN.2022.3192088

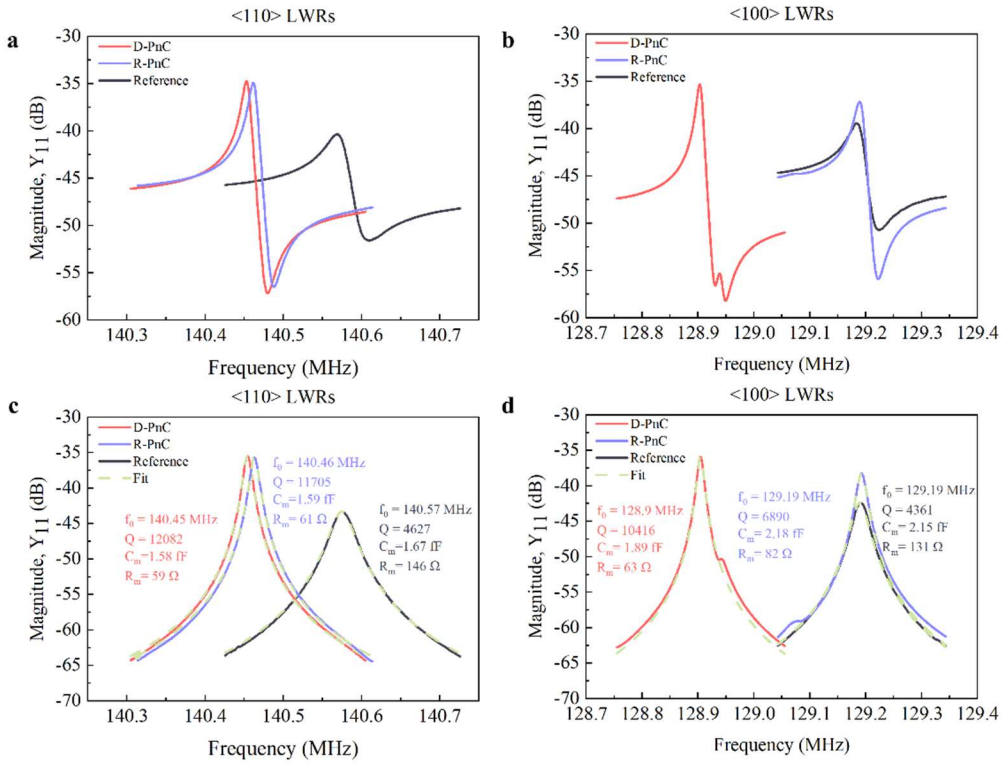

FIG. 5. Y_{11} admittance of each triplet of LWRs (LWR with D-PnC anchoring boundaries, LWR with R-PnC anchoring boundaries and a reference LWR with no PnC at the anchoring boundaries): a) LWRs aligned along the <110> axis and b) LWRs aligned along with the <100> axis. Corresponding Y_{11} spectra after removing feedthrough due to the static capacitance C_0: c) along the <110> axis where both PnC-bounded LWRs delivers Q of 12000 (double of the reference LWR), and d) aligned along with the <100> axis where only the LWR with D-PnC anchoring boundaries delivers a high Q of 10000 that is over double of the reference LWR while the LWR with R-PnC anchoring boundaries delivers a Q of 6900 that is only 1.5 times of the reference LWR.

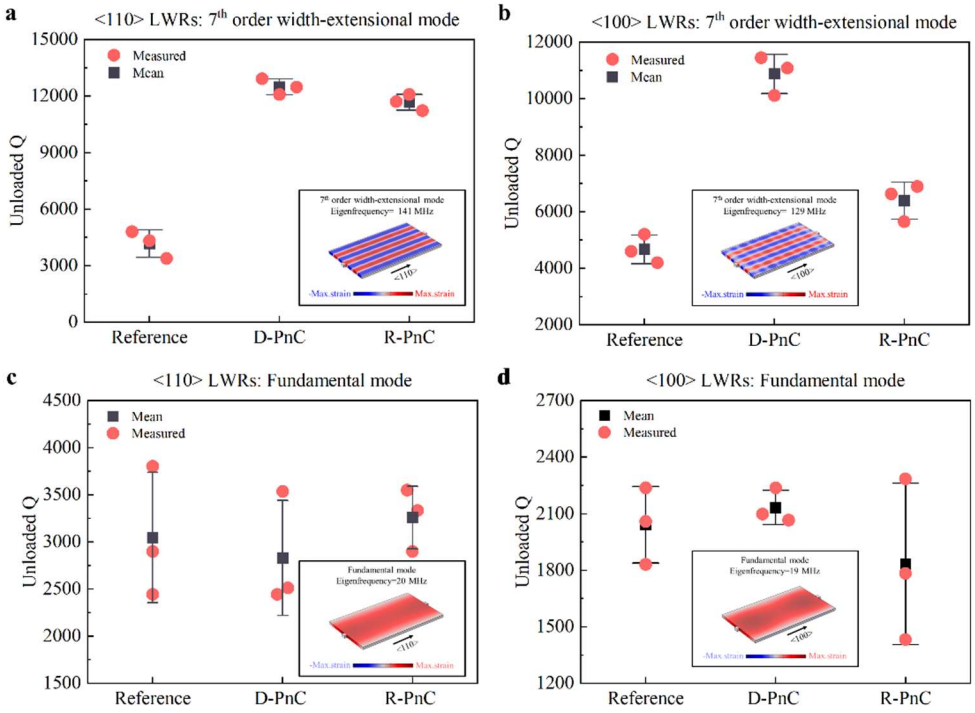

FIG. 6. Comparison of unloaded Q extracted from triplicate samples of each LWR variant in each of the crystal orientations tested transduced in the 7th order width-extensional mode: a) aligned along the <110> axis where both D-PnC and R-PnC boost Q to over 11000, b) aligned along the <100> axis where only the D-PnC provides the same significant boost to Q as the <110> LWRs. Error bars denote the standard deviation. Comparison of unloaded Q extracted from the same three LWRs transduced in the fundamental mode that lies far away from the theoretical ABG: Neither of the PnCs provides a distinct boost to Q for either the c) <110> axis alignment or d) <100> axis alignment. Error bars denote the standard deviation.

© 2022 IEEE. Personal use is permitted, but republication/redistribution requires IEEE permission. See https://www.ieee.org/publications/rights/index.html for more information.

This article has been accepted for publication in IEEE Sensors Journal. This is the author's version which has not been fully edited and content may change prior to final publication. Citation information: DOI 10.1109/JSEN.2022.3192088

LWR (i.e. 18 devices in all). Fig. 6(a-b) summarizes the extracted Q from each triplicate of LWRs. For the LWRs with D-PnC anchoring boundaries, the mean Q reaches 12500 along the <110> orientation and 10900 along the <100> orientation. Compared to other LWRs fabricated in the same process and of similar frequency, these levels of Q are on par with the highest values we have obtained so far. Where Q reaches the level of over 10000, we have shown that electrode-related losses dominate over anchor loss through extensive modeling [31]. For LWRs with R-PnC anchoring boundaries, the Q was boosted to over 11600 along the <110> orientation but only increases to 6400 along the <100> orientation. As such, the D-PnCs are unique in their effectiveness in boosting the Q of LWRs aligned along the main crystal orientations of (100) Si: <100> and <110>. We did not explore orientations between <100> and <110> due to the occurrence of multiple spurious according to FE simulations. Therefore, we have demonstrated that the D-PnCs can provide significant enhancement in Q for the LWRs along either the <110> or <100> orientation. In contrast, the R-PnCs can only provide an equivalent level of enhancement for the LWRs along <110> orientation.

To demonstrate that the PnCs only work inside the ABG, the same LWRs were transduced in the fundamental laterally vibrating mode. For the <110> direction, this occurs at 20 MHz, while for the <100> direction, the fundamental mode occurs at 19 MHz, which lie far beyond the ABG of either PnCs. Fig. 6(c-d) summarizes the extracted Qs once again from triplicate measurements of each LWR variant for both crystal axes. As expected from theory, neither the D-PnC nor R-PnC provides any Q-enhancement beyond the ABG along either orientation. As such, the measurement results of the LWRs at the intended 7th order width-extensional mode and at the fundamental mode show that the Q-enhancement by the PnCs is specific to the frequency range of the ABG associated with the PnCs.

IV. EXPERIMENTAL VERIFICATION: ATTENUATION THROUGH PNCS IN DELAY LINES

To compare the effect of orientation on the D-PnC to attenuate the acoustic transmission along each of the <110> and <100> axis, we designed and fabricated a pair of delay lines for

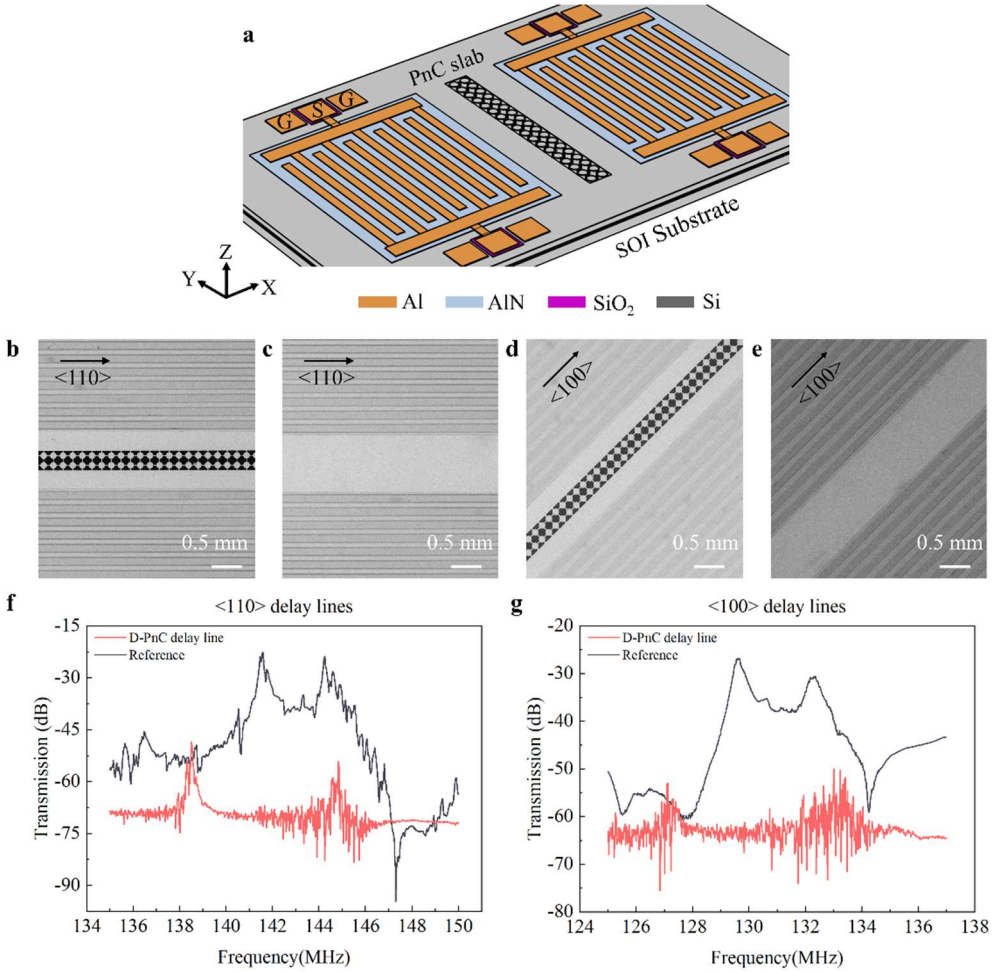

FIG. 7. (a) Schematic of a delay line with PnCs between the transmit and receive IDTs. SEM images of a fabricated delay line along <110> orientation with (b) D-PnCs in the transmission medium, and a reference delay line with only (c) a solid Si slab in the transmission medium. (d-e) The same delay lines were fabricated for <100> orientation. Measured electrical transmission (S_{21}) of a delay line incorporating D-PnCs compared against a reference delay line with a Si slab in the transmission medium: f) delay lines fabricated along the <110> direction (distinctive transmission band observable between 141-145 MHz) and g) delay lines fabricated along the <100> direction (distinctive transmission band from 129-132.5 MHz). In either direction alignments, the D-PnC provides an attenuation >50 dB (full extent masked by noise floor of the instrument).

© 2022 IEEE. Personal use is permitted, but republication/redistribution requires IEEE permission. See https://www.ieee.org/publications/rights/index.html for more information.

This article has been accepted for publication in IEEE Sensors Journal. This is the author's version which has not been fully edited and content may change prior to final publication. Citation information: DOI 10.1109/JSEN.2022.3192088

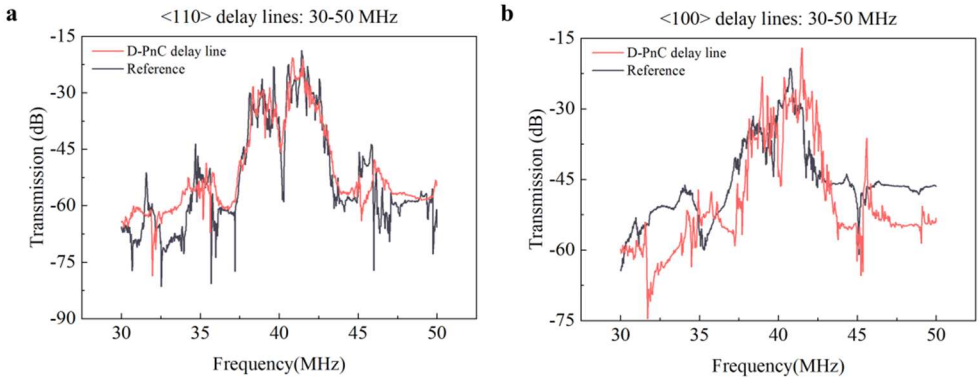

FIG. 8. Comparison of measured transmission (S_{21}) of delay lines with D-PnCs and reference delay lines with a Si slab in the transmission medium when transduced outside the theoretical acoustic band gap in the range of 30-50 MHz. a) Delay lines aligned along the <110> orientation; b) delay lines aligned along the <100> orientation. In either orientation alignment, the PnCs do not provide a clear attenuation to wave transmission relative to the reference delay line.

each orientation as shown in Fig. 7(a) (schematic). The pair of delay lines differ only by the defining feature in the transmission medium: D-PnC (Fig. 7(b) and (Fig. 7(d)) and a solid Si slab (Fig. 7(c) and (Fig. 7(e)) as reference delay lines to provide a baseline measurement. As such, a total of four delay lines were designed and fabricated to compare the transmission within and beyond the ABG frequency range of the D-PnC. As the D-PnC has a wide ABG, it is impractical to generate a sufficiently wide transmission through one delay line to cover the full span of the ABG [43]. As such, we utilized the same delay line to generate two limited spans to examine the attenuation inside and outside the ABG. The fabricated delay lines had a pair of standard interdigital differential transducers (IDTs) with a uniform W_p (30 µm as in the case of LWRs). Differential electrodes were employed to reduce parasitic electrical feedthrough by performing fully differential transmission measurements [31]. The IDTs were designed with 18 pairs of fingers with an aperture of 1 mm and the length of the transmission medium was set to 1 mm.

For the span inside the ABG, the delay lines are transduced within the designed center frequency (f_c) along the <110> and <100> directions respectively. Fig. 7(f) and Fig. 7(g) compare the measurement results for each pair of delay lines inside the respective ABG along either orientation. We can see that the Si slab delay line shows a distinctive transmission band spanning from 141-145 MHz with a low insertion loss (20 dB) around 142 MHz along the <110> orientation and a distinctive transmission band spanning from 129-133 MHz with a low insertion loss (26.8 dB) around 129 MHz along the <100> direction. The down shift in the transmission range corresponds to the difference in the phase velocity in silicon between the<110> and <100> directions. In the delay lines incorporating the D-PnCs, we see a huge contrast in the transmission relative to the reference delay lines for either orientation with a similar level of attenuation by 50 dB. These results further corroborate that the D-PnC design is insensitive to the change in orientation and thus exhibits excellent effectiveness in Q-boosting for LWRs aligned to either orientation as described in the previous section.

In addition to the span inside the ABG, the same set of delay lines were also transduced at much lower frequencies coinciding with the respective fundamental mode, which lies well outside the ABG for either orientation. The experimental results are shown in Fig. 8(a) for the alignment to the <110> direction and Fig. 8(b) for the alignment to the <100> direction. In either orientation, we see no visible difference in the transmission curve of the reference delay lines and the delay lines incorporating the D-PnC. As such, these results confirm that outside the ABG, the PnC no long prohibits the propagation of waves, which corroborates the results of the LWRs transduced in the fundamental mode. Outside the ABG, the PnC no longer confines the waves to the LWR resulting in Q that are not any higher than a reference LWR without PnCs at the anchoring boundaries.

V. CONCLUSION

In this work, we explored the effect of orientation on the acoustic band gap (ABG) of phononic crystals (PnC) to boost Q of AlN-on-Silicon Lamb Wave Resonators. Most reports on PnCs have focused on the commonly used <110> orientation. Here we studied the effect of changing the orientation of two PnC designs with respect to the ABG and Q-boost of LWRs. We have found that the ABG associated with the D-PnC is rather unique in orientation-insensitivity while simply adding a hole into D-PnC forming an R-PnC changes the ABG to be more sensitive to changes in orientation. Incorporating the D-PnCs into LWRs, we have shown that the D-PnC is equally effective in boosting Q of LWRs to over 11000 for both <110> and <100> orientations, a level where electrode-related losses dominate. In contrast, the R-PnC provides the same level of boost to Q only along the <110> orientation. The equal effectiveness of the D-PnC to boost Q of the LWR in either crystal axis has been further corroborated by measurements of delay lines incorporating these PnCs. The robustness of the D-PnC to different orientation alignments opens up the possibility to engineer resonators along different orientations towards low phase noise and low temperature coefficient of frequency (TCF) resonator-based oscillators.

© 2022 IEEE. Personal use is permitted, but republication/redistribution requires IEEE permission. See https://www.ieee.org/publications/rights/index.html for more information.

This article has been accepted for publication in IEEE Sensors Journal. This is the author's version which has not been fully edited and
content may change prior to final publication. Citation information: DOI 10.1109/JSEN.2022.3192088

VI. REFERENCES

[1] J. Zou, C. Lin, A. Gao and A. P. Pisano, "The Multi-Mode Resonance in AlN Lamb Wave Resonators," *J. Microelectromech. Syst.,* vol. 27, no. 6, pp. 973-984, Dec. 2018.

[2] A. Gao, K. Liu, J. Liang and T. Wu, "AlN MEMS filters with extremely high bandwidth widening capability," *Microsyst. Nanoeng,* vol. 6, no. 74, pp. 1-11, May. 2020.

[3] D. Chen, H. Zhang, J. Sun, M. Pandit, G. Sobreviela, Y. Wang, A. Seshia and J. Xie, "Feedthrough parasitic nonlinear resonance in micromechanical oscillators," *Appl. Phys. Lett.,* vol. 117, no. 13, pp. 133502, 2020.

[4] C. T. C. Nguyen, "MEMS technology for timing and frequency control," *IEEE Trans. Ultrason. Ferroelectr. Freq. Control,* vol. 54, no.2, pp. 251-270, Feb. 2007.

[5] D. Chen, J. Sun, M. Pandit, H. Zhang, G. Sobreviela, Y. Wang, X. Chen, A. Seshia and J. Xie, "Ultrasensitive resonant electrometry utilizing micromechanical oscillators," *Phys. Rev. Appl.,* vol. 14, no.1, pp.014001, Jul. 2020.

[6] R. Lu, M.H. Li, Y. Yang, T. Manzaneque, and S. Gong, "EME Accurate Extraction of Large Electromechanical Coupling in Piezoelectric MEMS Resonators," *J. Microelectromech. Syst.* vol. 28, no. 2, pp. 209-218, Apr. 2019.

[7] J. Zou, J. Liu and G. Tang, "Transverse Spurious Mode Compensation for AlN Lamb Wave Resonators," *IEEE Access*, vol. 7, pp. 67059-67067 Mar. 2019.

[8] D. A. Czaplewski, S. Strachan, O. Shoshani, S. W. Shaw and D. López, "Bifurcation diagram and dynamic response of a MEMS resonator with a 1:3 internal resonance," *Appl. Phys. Lett.,* vol. 114, pp. 254104, 2019.

[9] L. W. Hung and C. T. C. Nguyen, "Capacitive-Piezoelectric Transducers for High- Q Micromechanical AlN Resonators," *J. Microelectromech. Syst.,* vol. 24, no. 2 pp. 458-473, Apr. 2015.

[10] H. T. Jen, G. Pillai , S. I. Liu and S. S. Li, "High-Q Support Transducer MEMS Resonators Enabled Low-Phase-Noise Oscillators," *IEEE Trans. Ultrason. Ferroelectr. Freq. Control,* vol. 68, no. 4, pp. 1387 – 1398, Apr. 2021.

[11] S. A. Tella, N. Alcheikh and M. I. Younis, "A single MEMS resonator for reconfigurable multifunctional logic gates," *J. Micromech. Microeng.,* vol. 28, no.9, pp. 095002, May. 2018.

[12] Y. W. Lin, S. Lee, S. S. Li, Y. Xie, Z. Y. Ren, and C. T. C. Nguyen, "Series-resonant VHF micromechanical resonator reference oscillators," *IEEE J. Solid-State Circuits,* vol. 39, no. 12, pp. 2477-2491, Nov. 2004.

[13] R. Abdolvand, B. Bahreyni, J. E. Y. Lee, and F. Nabki, "Micromachined Resonators: A Review," *Micromachines,* vol.7, no. 9, pp. 160, Jun. 2016.

[14] M. Li, C. Chen, W. Chen and S. Li, "A Vertically Coupled MEMS Resonator Pair for Oscillator Applications," *J. Microelectromech. Syst.,* vol. 24, no. 3, pp. 528-530, Jun. 2015.

[15] R. Abdolvand, H. M. Lavasani, G. K. Ho, and F. Ayazi, "Thin-film piezoelectric-on-silicon resonators for high-frequency reference oscillator applications," *IEEE Trans. Ultrason. Ferroelectr. Freq. Control,* vol. 55, no. 12, pp. 2596-2606, Dec. 2008.

[16] Y. Yang, R. Lu, and S. Gong, "High Q Antisymmetric Mode Lithium Niobate MEMS Resonators with Spurious Mitigation," *J. Microelectromech. Syst.,* vol. 29, no.2 pp. 135-143, Feb. 2020.

[17] J. M. Lehto Miller1, A. Ansari, D. B. Heinz1, Y. Chen, I. B. Flader, D. D. Shin, L. G. Villanueva and T. W. Kenny1, "Effective quality factor tuning mechanisms in micromechanical resonators," *Appl. Phys. Rev.,* vol. 5, no. 4, pp. 041307, Dec. 2018.

[18] G. Piazza, P. J. Stephanou, and A. P. Pisano, "Piezoelectric Aluminum Nitride Vibrating Contour-Mode MEMS Resonators," *J. Microelectromech. Syst.* vol. 15, no. 6, pp. 1406-1418, Dec. 2006.

[19] G. K. Ho, R. Abdolvand, A. Sivapurapu, S. Humad, and F. Ayazi, "Piezoelectric-on-Silicon Lateral Bulk Acoustic Wave Micromechanical Resonators," *J. Microelectromech. Syst.,* vol. 17, no.2, pp. 512-520, Apr. 2008.

[20] J. E. Y. Lee, J. Z. Yan, and A. A. Seshia, "Study of lateral mode SOI-MEMS resonators for reduced anchor loss,"*J. Micromech. Microeng.,* vol. 21, no. 4, pp. 045010, Mar. 2011.

[21] M. W. U. Siddiqi, P. Fedeli, C. Tu, A. Frangi and J. E. Y. Lee, "Numerical analysis of anchor loss and thermoelastic damping in piezoelectric AlN-on-Si Lamb wave resonators," *J. Micromech. Microeng.,* vol. 29, no. 10, pp. 105013, Aug. 2019.

[22] K. N. B. Narayanan, D. R. Nair and A. Dasgupta, "Design, Modeling and Fabrication of TPoS MEMS Resonators with Improved Performance at 1 GHz," *J. Microelectromech. Syst.,* vol. 30, no. 3, pp. 375-383, Jun. 2021.

[23] X. Y. Li, Y. L. Huang, Y. J. Du, Z. P. Li, F. H. Bao and J. F. Bao, "Study of a 10 MHz MEMS oscillator with a TPoS resonator," *Sens. Actuator A Phys.,* vol. 258, no. 1, pp. 59-67, May. 2017.

[24] Shahmohammadi, M., H. Fatemi, and R. Abdolvand, "Nonlinearity reduction in silicon resonators by doping and re-orientation," in *MEMS,* Taipei, Taiwan, 2013, pp. 793-796.

[25] M. Shahmohammadi, B. P. Harrington, and R. Abdolvand, "Turnover Temperature Point in Extensional-Mode Highly Doped Silicon Microresonators," *IEEE Trans. Electron Devices,* vol. 60, no. 3, pp. 1213-1220, Mar. 2013).

[26] R. Janna, S. A. Chandorkar, C.A. Watson, G. M. Glaze, C. H. Ahn, E. J. Ng, Y. Yang, and T. W. Kenny. "Direct Detection of Akhiezer Damping in a Silicon MEMS Resonator," *Sci. Rep.,* vol. 9, pp. 1-10, Feb. 2019.

[27] A. Qamar, S. Sherrit, X. -Q. Zheng, J. Lee, P. X. -L. Feng and M. Rais-Zadeh, "Study of Energy Loss Mechanisms in AlN-Based Piezoelectric Length Extensional-Mode Resonators," *J. Microelectromech. Syst.,* vol. 28, no. 4, pp. 619-627, Aug. 2019.

[28] C. M. Lin, Y. J. Lai, J. C. Hsu, Y. Y. Chen, D. G. Senesky, and A. P. Pisano, "High-Q aluminum nitride Lamb wave resonators with biconvex edges," *Appl. Phys. Lett.,* vol. 99, pp. 143501, Oct. 2011.

[29] L. Binci, C. Tu, H. Zhu, and J. E. Y. Lee, "Planar ring-shaped phononic crystal anchoring boundaries for enhancing the quality factor of Lamb mode resonators," *Appl. Phys. Lett.,* vol. 109, pp. 203501, Nov. 2016.

[30] C. Tu and J. E. Y. Lee, "Enhancing quality factor by etch holes in piezoelectric-on-silicon lateral mode resonators," *Sens. Actuator A Phys.,* vol. 259, no. 1, pp. 144-151, Jun. 2017.

[31] M. W. U. Siddiqi and J. E. Y. Lee, "Wide Acoustic Bandgap Solid Disk-Shaped Phononic Crystal Anchoring Boundaries for Enhancing Quality Factor in AlN-on-Si MEMS Resonators," *Micromachines,* vol. 9, no. 8, pp. 413, Aug. 2018.

[32] T. B. Workie, T. Wu, J. F. Bao and K. Y. Hashimoto, "Design for high-quality factor of piezoelectric-on-silicon MEMS resonators using resonant plate shape and phononic crystals," *Jpn. J. Appl. Phys.*, vol. 60, no. SD, pp. SDDA03, Mar. 2021.

[33] B. Hamelin, J. Yang, A. Daruwalla, H. Wen and F. Ayazi, "Monocrystalline Silicon Carbide Disk Resonators on Phononic Crystals with Ultra-Low Dissipation Bulk Acoustic Wave Modes," *Sci. Rep.,* vol. 9, no. 1, pp. 1-8, Dec. 2019.

[34] F. Gao, A. Bermak, S. Benchabane, R. Laurent and K. Abdelkrim, "Acoustic radiation-free surface phononic crystal resonator for in-liquid low-noise gravimetric detection," *Microsyst. Nanoeng.,* vol. 7, pp. 8, Jan. 2021.

[35] A. Khelif, and A. Adibi., "Fundamental Properties of Phononic Crystal," in *Phononic crystals*, Berlin, Germany, *Springer*, 2015, pp.31-35.

[36] W. Kuang, Z. Hou, and Y. Liu, "The effects of shapes and symmetries of scatterers on the phononic band gap in 2D phononic crystals," *Phys. Lett. A* vol. 332, no. 5-6, pp.481-490, Nov. 2004.

[37] J. Dhillon, A. Bozhko, E. Walker, A. Neogi and A. Krokhin, "Localization of ultrasound in 2D phononic crystal with randomly oriented asymmetric scatterers," *J. Appl. Phys.,* vol. 129, pp. 134701, Apr. 2021.

[38] Z. Zhang, X. K. Han, and G. M. Ji. "The bandgap controlling by geometrical symmetry design in hybrid phononic crystal," *Int. J. Mod. Phys. B,* vol. 32, no. 4, 041850034, 2018.

[39] J. Chen, H. Huang, S. Huo, Z. Tan, X. Xie, J. Cheng and G. Huang, "Self-ordering induces multiple topological transitions for in-plane bulk waves in solid phononic crystals," *Phys. Rev. B,* vol. 98, no. 1, pp. 014302, Jul. 2018.

[40] R. Yang, J. Qian, and J. E. Y. Lee, "Boosting Q of <100> Aligned ALN-on-Silicon Laterally Vibrating Resonators by Wide Acoustic Bandgap Phononic Crystal Anchors," in *Transducers,* Online, 2021, pp. 1375-1378.

[41] A. Cowen, G. Hames, K. Glukh, and B. Hardy, "PiezoMUMPs™ Design Handbook," *MEMSCAP Inc.,* Version 1.3, pp. 4-9, Durham, NC, USA, 2014.

[42] M. Sledzinska, B. Graczykowski, J. Maire, E. Chavez-Angel, C. M. Sotomayor-Torres, and F. Alzina, "2D phononic crystals: Progress and prospects in hypersound and thermal transport engineering." Advanced Functional Materials, 30, no.8, pp. 1904434. 2020.

[43] J. C. Hsu and F. S. Lin, "Measurement of locally resonant band gaps in a surface phononic crystal with inverted conical pillars." Jpn. J. Appl. Phys. vol. 57, no. 07LB01, pp. 07LB01, Apr. 2018.

© 2022 IEEE. Personal use is permitted, but republication/redistribution requires IEEE permission. See https://www.ieee.org/publications/rights/index.html for more information.